Metals & corrosion

Effect of plasma remelting on microstructure and properties of a CoCrCuNiAl$_{0.5}$ high-entropy alloy prepared by spark plasma sintering

Mingliang Wang[1], Guojia Zhang[1], Hongzhi Cui[2,*], Yiping Lu[1,*] (iD), Yong Zhao[2],
Na Wei[2], and Tingju Li[1]

[1] Key Laboratory of Solidification Control and Digital Preparation Technology (Liaoning Province), School of Materials Science and Engineering, Dalian University of Technology, Dalian 116024, People's Republic of China
[2] School of Materials Science and Engineering, Shandong University of Science and Technology, Qingdao 266590, People's Republic of China

ABSTRACT

A CoCrCuNiAl$_{0.5}$ high-entropy alloy (HEA) was prepared by spark plasma sintering (SPS). The effect of plasma transferred arc (PTA) remelting on the microstructures and properties of the SPS-ed HEA was studied. The results showed that, after PTA remelting, the microstructures transformed from randomly-oriented equiaxed grains to dendrites with a directional solidified morphology. The coarse plate-like precipitates (~ 130 nm in diameter and ~ 20 nm in thickness) containing ordered L1$_2$ and disordered FCC structures inside the matrix grains were replaced by the disordered FCC spherical Cu-rich precipitates with several nanometers within the dendritic matrix. In the intergranular region, the size of the L1$_2$ cubic precipitates was decreased from ~ 55 nm to ~ 2 nm, and dislocations and lattice distortions were also observed. In addition, the brittle B2 phase was disappeared, and the extent of Cu segregation was decreased in the interdendritic region. The SPS-ed sample has a compressive yield strength of 913.8 MPa and a fracture strain of 21.7%. However, the PTA remelted sample exhibits a much higher fracture strain ($> 70\%$, without fracture) and an appreciable yield strength of 739.4 MPa, which indicates an excellent balance between strength and ductility was achieved after PTA remelting. Furthermore, the corrosion resistance of the PTA remelted sample was higher than that of the SPS-ed sample, which was mainly due to the decreased elemental segregation, and the reduced sizes and types of the precipitates.

GRAPHICAL ABSTRACT
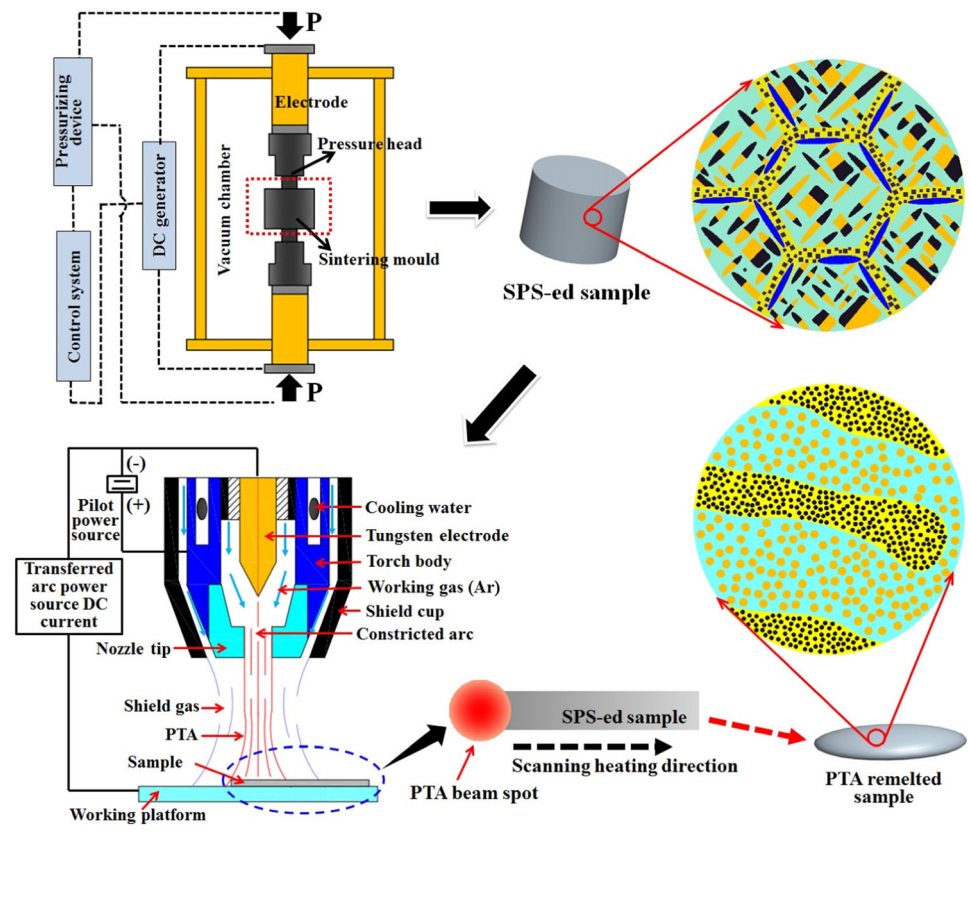
Introduction

The concept of high-entropy alloy (HEA), which was originally defined based on the viewpoint that high mixing entropy was in favor of the formation of a single solid solution phase, was put forward by Yeh et al. in 2004 [1]. The HEA design strategy indicates that the range of alloy design extends to the central regions of multi-element phase diagrams, which leads to a significant increase in the degree of compositional freedom. This can promote the creation of a series of new alloys with unique combinations of properties that are significantly superior to the conventional alloys, such as high strength [2–4], high hardness [5, 6], strong fatigue and fracture resistance [7–9], good thermal stability [10–12], excellent wear resistance [13–15], superior corrosion resistance

[16–19], attractive electrical and magnetic properties [20–22], and excellent irradiation resistance [23–25].

Currently, most of the reported HEAs were usually fabricated by vacuum arc melting, and the final products have limited sizes and shapes with shrinkage defects and elemental segregation in their as-cast state, which has restricted their industrial applications. Spark plasma sintering (SPS), which can rapidly consolidate powders and obtain high densities by applying pressure and passing an electric pulse current, is a promising method for the fabrication of high-performance HEA materials. Thus, an increasing number of HEA systems with excellent properties have been prepared by using SPS directly in recent reports [6, 14, 26, 27]. However, the lower cooling rate after SPS (furnace cooling under vacuum) generally contributes to the formation of stable phases in HEAs [26, 27]. This can often result

in the coarse precipitates with different sizes [6], which leads to the decrease in ductility. Some processing technologies, such as rolling [28–30], high-pressure torsion [31, 32], rotary friction welding [33], and friction stir processing [34], may be used to improve the microstructures, but these methods are usually complex and time-consuming.

Rapid remelting technology with high-energy sources, such as laser, electron, and plasma beams, is accomplished by rapidly traversing a continuous, high-energy–density beam over a material to produce a rapid solidified microstructure. The remelted microstructures often exhibit refinement, reduced cracks and porosities, and more uniform phase distributions, which improve their overall properties [35–37]. Although laser remelting has been widely applied, the energy transfer efficiency of laser is relatively low, and its application is limited by the expensive equipment [38–40]. In addition, obtaining an electron beam with the required intensity is difficult, and the application of an electron beam usually requires a vacuum environment [37, 40]. Compared to laser and electron beams, plasma beam with an excellent stability, a high energy exchange efficiency and a low cost of equipment, is more suitable for large-scale industrial applications [39, 41, 42]. Furthermore, the temperature and energy density of the plasma transferred arc (PTA) can reach $20,000 - 30,000$ °C and $10^5 - 10^6$ W/cm^2, respectively [38, 43]. Thus, high cooling rates of about 10^4–10^8 K/s during the nonequilibrium solidification can be achieved. Although PTA was widely used to prepare coatings [39, 41–43], there have been no reports about the effect of PTA remelting on the microstructures and properties for the HEAs subjected to SPS.

In this work, a CoCrCuNiAl$_{0.5}$ HEA, which contains intricate precipitated phases with different sizes after SPS in our preliminary observations, was selected to investigate the microstructural evolution before and after PTA remelting. The bulk CoCrCuNiAl$_{0.5}$ HEA was fabricated by using SPS first, and then the machined thin samples were remelted via a plasma machine with an optimized remelting parameter. The effect of PTA remelting on the microstructures and properties of the SPS-ed HEA was studied.

Experimental procedure

Preparation of the HEA samples.

Co, Cr, Cu, Ni, and Al metal powders with particle sizes of $\sim$ 44 μm (-325 mesh) and purity > 99.8 wt% were used to fabricate CoCrCuNiAl$_{0.5}$ (mol%) samples. The powders were blended for 10 h using a planetary ball-mill and protected by argon. An SPS-332LX device (Fuji Radio Engineering Machinery Co. Ltd., Japan) was used to consolidate the mixed powders into bulk samples at 1050 °C for 8 min with a heating rate of 70 °C/min and a constant pressure of 30 MPa (Fig. 1a), followed by furnace cooling. The vacuum pressure was kept at < 10 Pa during SPS. Following SPS, the SPS-ed samples with size of $\varnothing 20 \times 10$ mm were obtained, as shown in Fig. 1b. The SPS-ed samples for subsequent testing and PTA remelting experiments were sectioned by electrical discharge machining.

The SPS-ed samples for PTA remelting experiments were cut into rectangular sheets with sizes of $15 \times 2.5 \times 1.0$ mm, as displayed in Fig. 1c. The surfaces of the processed samples were polished to remove oxide. The PTA remelting experiments were performed using a homemade plasma machine [39]. The operating principle of the PTA remelting system was schematically shown in Fig. 1d. During remelting, PTA with a high energy density was ignited, and the PTA beam diameter was 4 mm. The surface of 15×2.5 mm of the SPS-ed sample was heated along the direction of length, from one end to the other, as shown in Fig. 1e. The diameter of the PTA beam (4 mm) was larger than the width of the sample (2.5 mm), and the sample thickness was only 1.0 mm. This ensured that that the SPS-ed samples were thoroughly remelted after a single-pass heating. During remelting, argon was used as the working and shielding gas to prevent surface contamination. The optimized PTA remelting parameters are listed in Table 1. The remelted samples for subsequent characterization were also cut by electrical discharge machining.

Characterization

A D/Max 2500 PC Rigaku X-ray diffractometer (XRD) with a Cu Kα radiation (λ = 0.15405 nm) was used to analyze the phase constituents of the samples. Microstructures were characterized in an FEI Nova NANOSEM 450 scanning electron microscope
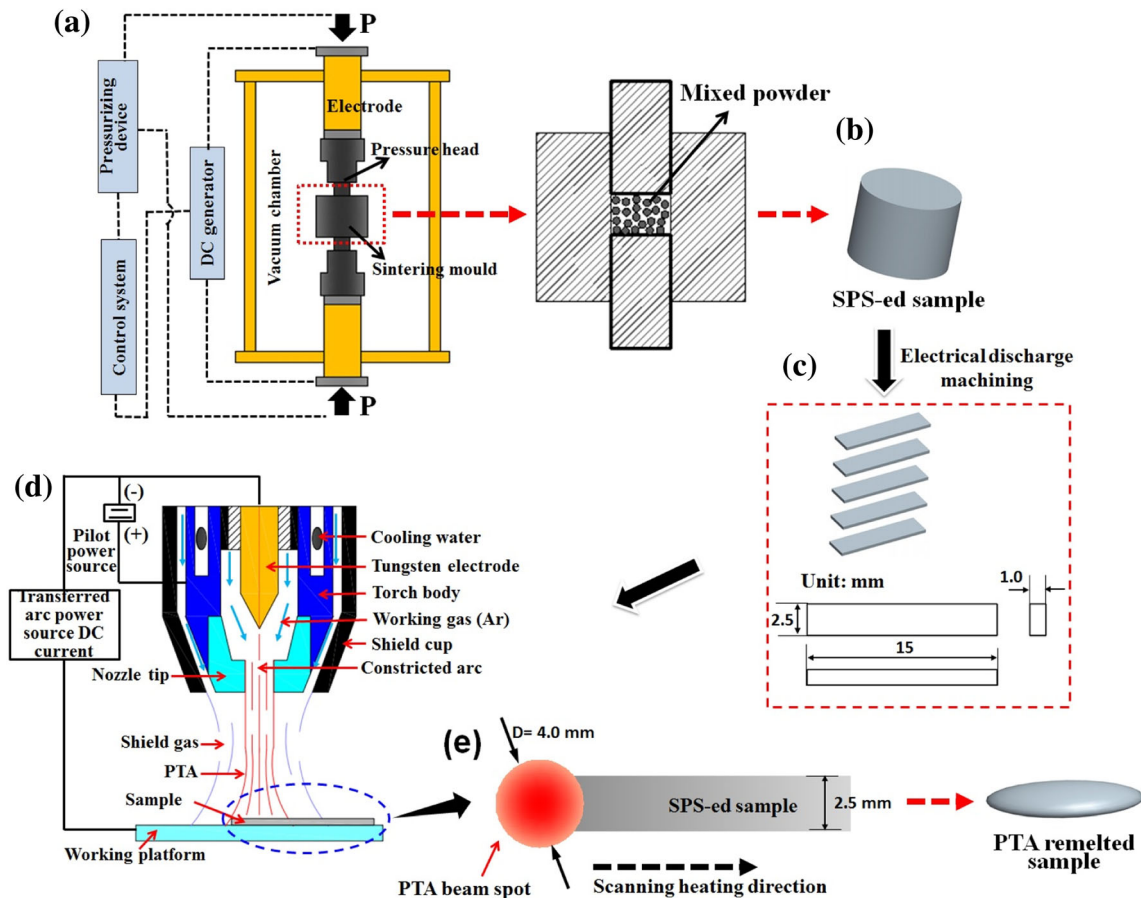
Figure 1 Schematic drawings of the HEA preparation procedure. **a** Bulk sample fabricated by SPS. **b** The SPS-ed bulk sample. **c** Sizes of the machined SPS-ed sample. **d** The operating principle of the PTA remelting system. **e** PTA scanning heating process.

Table 1 The optimized PTA remelting parameters

Working current (A)	Working voltage (V)	Scanning speed (mm/s)	Working gas flux (Ar, l/min)	Shielding gas flux (Ar, l/min)	Working distance (mm)
100	30	80	5	6	8

(SEM), and energy-dispersive X-ray spectroscopy (EDS, INCAR, OXFORD) was applied to analyze the chemical compositions. The polished surfaces of both types of samples were studied by electron backscatter diffraction (EBSD) (XL-30 FEG FEI Philips), and the EBSD data were obtained by Orientation Imaging Microscopy hardware and were analyzed by the HKL Channel 5 software. Transmission electron microscopy (TEM) studies were performed on an FEI Tecnai G2 F20 S-TWIN operated at 200 kV. The chemical compositions of the nanoprecipitates were measured by a Super-X EDS detector equipped on an FEI-TITAN G2 TEM operating in a high-angle annular dark-field scanning TEM (HAADF-STEM) at 300 kV. An FEI Helios Nanolab 600i dual-beam focused ion beam (FIB) apparatus was used to fabricate the TEM foils. Compression tests were carried out utilizing an Instron 5500 testing system at a constant strain rate of 1×10^{-3} s^{-1} at ambient temperature. The size of compression test samples was $\Phi 3$ mm $\times$ 4.5 mm. For each sample type, at least five samples were tested to confirm the reproducibility and reliability of the results. Potentiodynamic polarization and electrochemical impedance spectroscopy

(EIS) tests were performed on an electrochemical workstation (Model: Reference 3000, Gamry) with a three-electrode system. The sample (0.3 cm^2), a platinum plate and a standard saturated calomel electrode (SCE) were the working electrode, counter electrode and reference electrode, respectively. The tests were performed in the 3.5 wt% NaCl solution at room temperature. The potentiodynamic curves were recorded at a sweep rate of 1 mV/s. The EIS tests were conducted at an alternating current frequency ranging from 10^5 Hz to 10^{-2} Hz. In order to guarantee the corresponding reproducibility, each test was repeated at least three times.

Results

XRD, SEM and EBSD studies

Figure 2a shows the XRD patterns of both the 0 h (as-blended) and 10 h milled powders. Diffraction peaks corresponding to all of the elemental components are evident in both patterns. A comparison of the two diffraction patterns indicates that there are almost no differences in the number and intensity of the diffraction peaks, which indicates that the mechanical alloying may not occur during ball milling. Note that, it is rational that the lower rotational speed (250 rpm) and the relatively short time (10 h) of ball milling would not lead to the mechanical alloying.

Figure 2b shows the XRD patterns of both the SPS-ed and PTA remelted samples. The XRD pattern of the SPS-ed sample is consisted of a primary disordered face-centered cubic (FCC) phase, an ordered FCC (L1$_2$) phase, and an ordered body-centered cubic (BCC) (B2) phase. The superlattice diffraction peaks (SDPs) at $2\theta = 24.8°$ and $35.1°$ are attributed to the respective (100) and (110) planes of the ordered L1$_2$ phase, while the SDP at $2\theta = 31.2°$ is ascribed to the respective (100) plane of the ordered B2 phase. After PTA remelting, only two diffraction peaks at $2\theta = 43.4°$ and $50.7°$ are observed in the XRD pattern, which are respectively attributed to the (111) and (200) planes of the disordered FCC phase. Additionally, the shift in the primary FCC diffraction peaks to left after PTA remelting is observed, which can also be seen clearly in the magnified image of the diffraction patterns at $2\theta = 48-53°$ (inset in Fig. 2b), indicating the extended solid solubility of the FCC solid solution in the PTA remelted sample.

The backscattered electron (BSE) image in Fig. 3a reveals that the SPS-ed sample possesses a polygonal equiaxed grain structure. The high-magnification BSE image (Fig. 3c) indicates that the SPS-ed sample contains a matrix grain phase, a white phase distributes in the intergranular region and a gray phase distributes between the matrix grain and the white phase. The measured compositions (atomic percent) of various phases in the SPS-ed sample (based on the SEM–EDS) indicate the matrix grains are rich in Cr
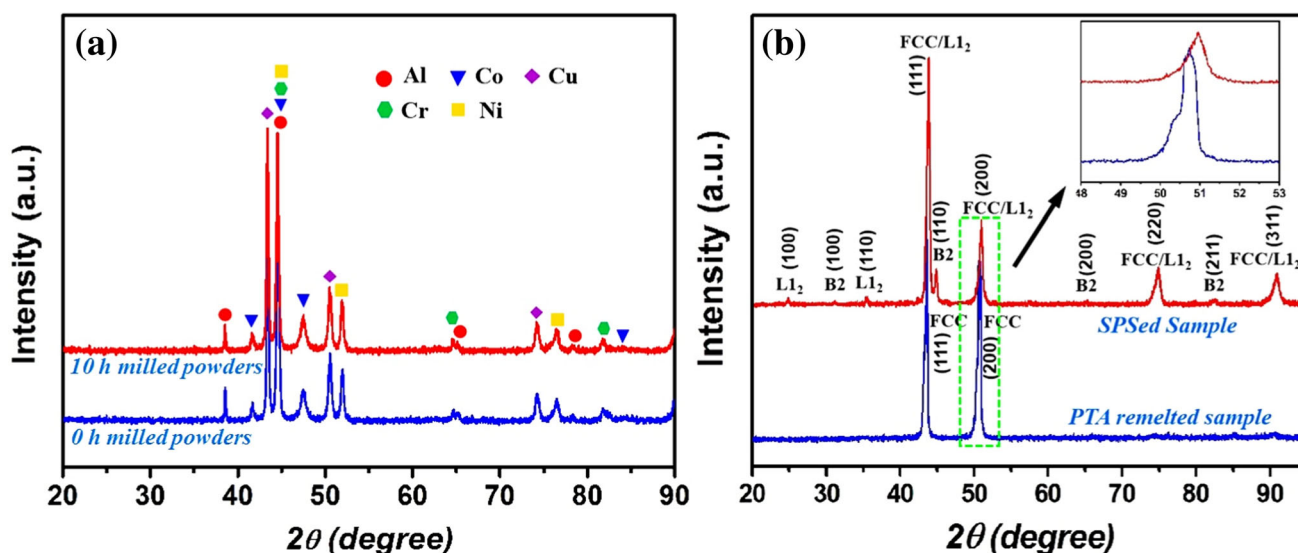
Figure 2 **a** XRD patterns of the mixed powders. **b** XRD patterns of the SPS-ed and PTA remelted samples. Inset shows the diffraction patterns at $2\theta = 48-53°$.

Figure 3 SEM images and EDS analyses of the HEA samples. **a** SEM image of the SPS-ed sample. **b** SEM image of the PTA remelted sample. **c** A high-magnification BSE image of the SPS-ed sample. c_1–c_5 EDS elemental distribution maps corresponding (**c**) showing Al, Ni, Cu, Cr and Co, respectively. **d** A high-magnification BSE image of the PTA remelted sample. d_1–d_5 EDS elemental distribution maps corresponding (**d**) showing Al, Ni, Cu, Cr and Co, respectively.
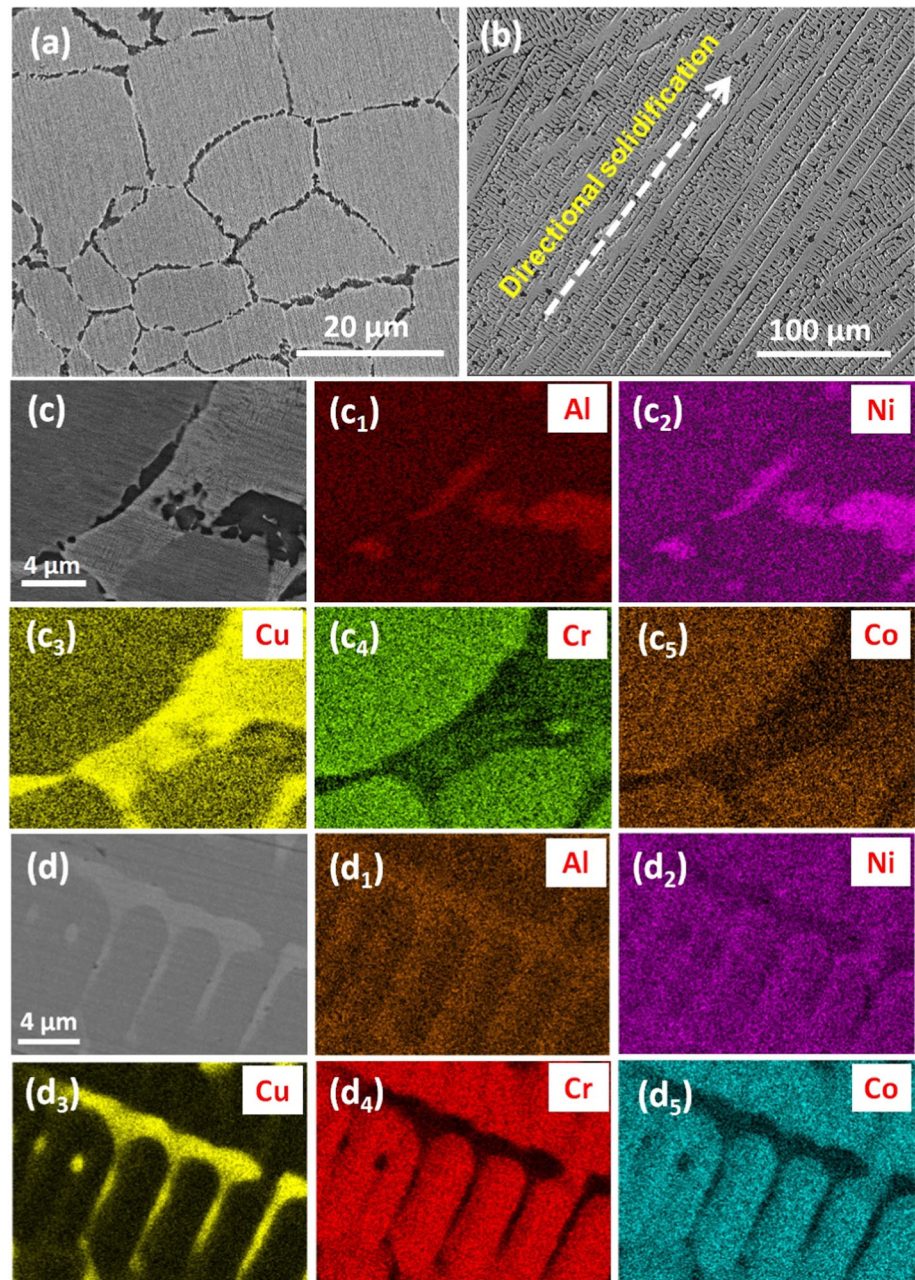
(30.62 at.%) and Co (30.19 at.%), the white phase is rich in Cu (76.54 at.%), while the gray phase is rich in Ni (37.56 at.%) and Al (34.98 at.%). The EDS elemental distribution maps (Fig. 3c_1–c_5) corresponding to Fig. 3c further substantiate the above EDS compositional analysis results.

After PTA remelting, the microstructure is transformed from an equiaxed to a dendritic structure with a directional solidified morphology, as shown in Fig. 3b. The high-magnification BSE image (Fig. 3d) and EDS maps of various elements (Fig. 3d_1–d_5) reveal that the PTA remelted sample is composed of only a dendritic matrix phase (27.46 at.% Co, 28.57 at.% Cr, 12.45 at.% Cu, 22.36 at.% Ni, 9.16 at.% Al) and an interdendritic white phase (66.03 at.% Cu, 13.63 at.% Ni, 10.77 at.% Al, 5.88 at.% Co, 3.69 at.% Cr). Similar to the SPS-ed sample, the dendritic matrix phase is also rich in Co and Cr, and the interdendritic phase is Cu rich; however, the gray Ni–Al-rich phase is not observed in the PTA remelted sample. In addition, compared with the SPS-ed sample, the size of the Cu-rich phase in the

interdendritic region of the PTA remelted sample is much finer. The mean widths of the Cu-rich phase perpendicular to the grain boundaries of the SPS-ed and PTA remelted samples were analyzed by using ImageJ software, and the results are approximately 4.5 μm and 1.3 μm, respectively. Furthermore, the measured Cu content in the interdendritic region of the PTA remelted sample (66.03 at.%) is much lower than that of the SPS-ed sample (76.54 at.%), which indicates that Cu segregation is decreased after PTA remelting.

The XRD results (Fig. 2b) indicate that the primary matrix phase has an FCC structure in both samples; thus the Orientation Imaging Microscopy was used to acquire the FCC grain information. Figure 4 shows the EBSD inverse pole figures (IPFs) over a large scanning area (1000 × 1002 μm) for both samples. The IPF of the SPS-ed sample (Fig. 4a) reveals that the equiaxed grains have a random orientation; however, the PTA remelted sample (Fig. 4b) exhibits the preferential growth along the (111) and (001) planes, in agreement with the XRD analysis (Fig. 2b).

TEM analysis

As shown in the bright-field (BF) TEM image (Fig. 5a), the SPS-ed sample is composed of the matrix grain phase, Ni–Al-rich phase, and an intergranular Cu-rich phase (confirmed by TEM-EDS), which is consistent with the SEM observations (Fig. 3). Selected area diffraction pattern (SADP) of the Ni–Al-rich phase along the [100] zone axis (Fig. 5a inset) exhibits reflections of an ordered BCC, which demonstrates that this phase has a B2 structure, corresponding to the diffraction peaks of the B2 phase, as marked in Fig. 2b. Figure 5b shows a BF TEM image of the matrix grain, which exhibits a high density of plate-like precipitates with diameters of approximately 130 nm and a mean thickness of 20 nm. SADPs obtained from the matrix grain along the $< 001 >$, $< 011 >$, and $< 111 >$ zone axes are shown in Fig. $5c_1$, c_2, and c_3, respectively. These SADPs reveal that the matrix has an FCC structure (γ), and the existence of {001} and/or {011} superlattice reflections indicates the presence of an ordered $L1_2$ phase (γ'). STEM-EDS mapping analysis (Fig. $5d_1$–d_8) along the $< 001 >$ zone axis reveals that each of the plate-like precipitates is composed of two regions: one enriched with Cu (containing 90.42 at.%

Cu confirmed by STEM-EDS) and the other enriched with Cu–Ni–Al (Cu, Ni and Al comprise 92.50 at.% of its composition).

The dark-field (DF) TEM image (Fig. 6a) made from the {100} superlattice spot in the SADP (Fig. $5c_1$) reveals that the Cu-rich region of the plate-like precipitate exhibits a dark contrast, while the Ni–Al–Cu-rich region exhibits a bright contrast. This indicates that the Cu-rich region has a disordered structure, and the Ni–Al–Cu-rich region possesses an ordered $L1_2$ structure. The HRTEM image (Fig. 6b) and the corresponding electron diffraction patterns of the Ni–Al-Cu-rich region (Fig. 6c), matrix (Fig. 6d), and Cu-rich region (Fig. 6e) from Fast Fourier Transform (FFT) of Fig. 6b also reveal that both the γ matrix and Cu-rich region (further termed as Cu-plate) exhibit the disordered FCC structure, while the Ni–Al-Cu-rich region (further termed as γ_p') exhibits the ordered $L1_2$ structure. Further observation of the HRTEM image in Fig. 6b indicates that the atomic planes across the interfaces of Cu-plate/γ_p', γ_p'/γ matrix and γ matrix/Cu-plate are all continuous, suggesting the three phases are coherent. Moreover, the three phases have similar lattice constants measured by using the HRTEM images, with a maximum difference of approximately 2.1%, which is small enough to be readily accommodated by elastic strains.

SADPs, recorded from the intergranular Cu-rich phase in Fig. 5a, which can be indexed as $< 001 >$ and $< 114 >$ zone axes of the FCC structure, are shown in Fig. 7a and 7b, respectively. Note that the existence of {001} and/or {011} superlattice reflections in Fig. 7a and 7b also indicates that the presence of an $L1_2$ ordered phase inside the intergranular Cu-rich phase. The DF TEM image made from the {100} superlattice spot in the SADP (Fig. 7a) clearly reveals that the presence of cubic precipitates with bright contrast is dispersed in the matrix. The mean equivalent diameter of the cubic precipitates was analyzed by ImageJ software and was determined to be $\sim$ 55 nm. Both the HRTEM image (Fig. 7d) and the corresponding electron diffraction patterns of the cubic precipitate (Fig. 7e) and the matrix (Fig. 7f) from FFT of Fig. 7d reveal that the cubic precipitates possessing an ordered $L1_2$ structure are coherent with the matrix that has a disordered FCC structure. The Al, Ni, and Cu STEM-EDS maps (Fig. 7g-i, respectively) of the intergranular Cu-rich phase, reveal that the cubic precipitates are rich in Ni–Al (containing 45.30 at.%

Figure 4 EBSD characterization of the FCC matrix grains. **a** Inverse pole figure (IPF) map of SPS-ed sample. **b** IPF map of PTA remelted sample.
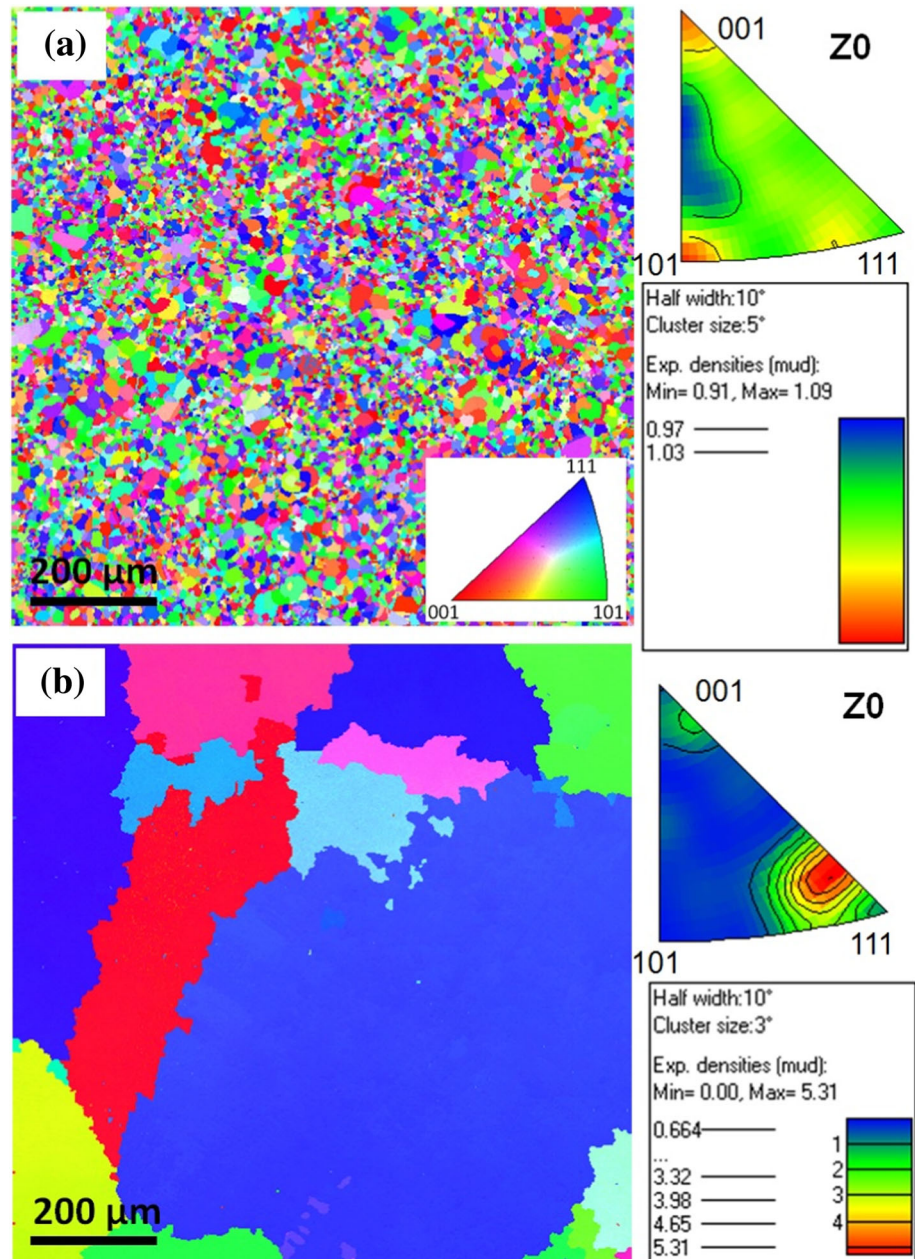

Ni and 20.34 at.% Al) relative to the matrix that is rich in Cu (containing 87.53 at.% Cu, subsequently termed as Cu matrix).

The above detailed characterization on SPS-ed sample suggests that, the matrix grains contain the disordered γ matrix, the ordered γ_P' and the disordered Cu-plate phases. The intergranular Cu-rich region consists of a principal disordered Cu matrix containing the dispersed ordered L1$_2$ cubic precipitates. The γ matrix, Cu-plate, and Cu matrix have similar lattice constants and all possess a disordered FCC structure, which makes them difficult to distinguish in the XRD patterns (Fig. 2b). Similarly, the γ_P' and the cubic precipitates have nearly the same lattice constants and both have the ordered L1$_2$ structure, leading to a set of diffraction peaks of ordered L1$_2$ in the XRD pattern.

As shown in Fig. 8a, a BF TEM image reveals that the PTA remelted sample is only composed of a dendritic matrix phase and an interdendritic Cu-rich phase, which is consistent with the SEM observations. SADPs along the < 001 > and < 112 > zone axes (Fig. 8b and 8c, respectively) obtained from the dendritic matrix phase exhibit reflections of a
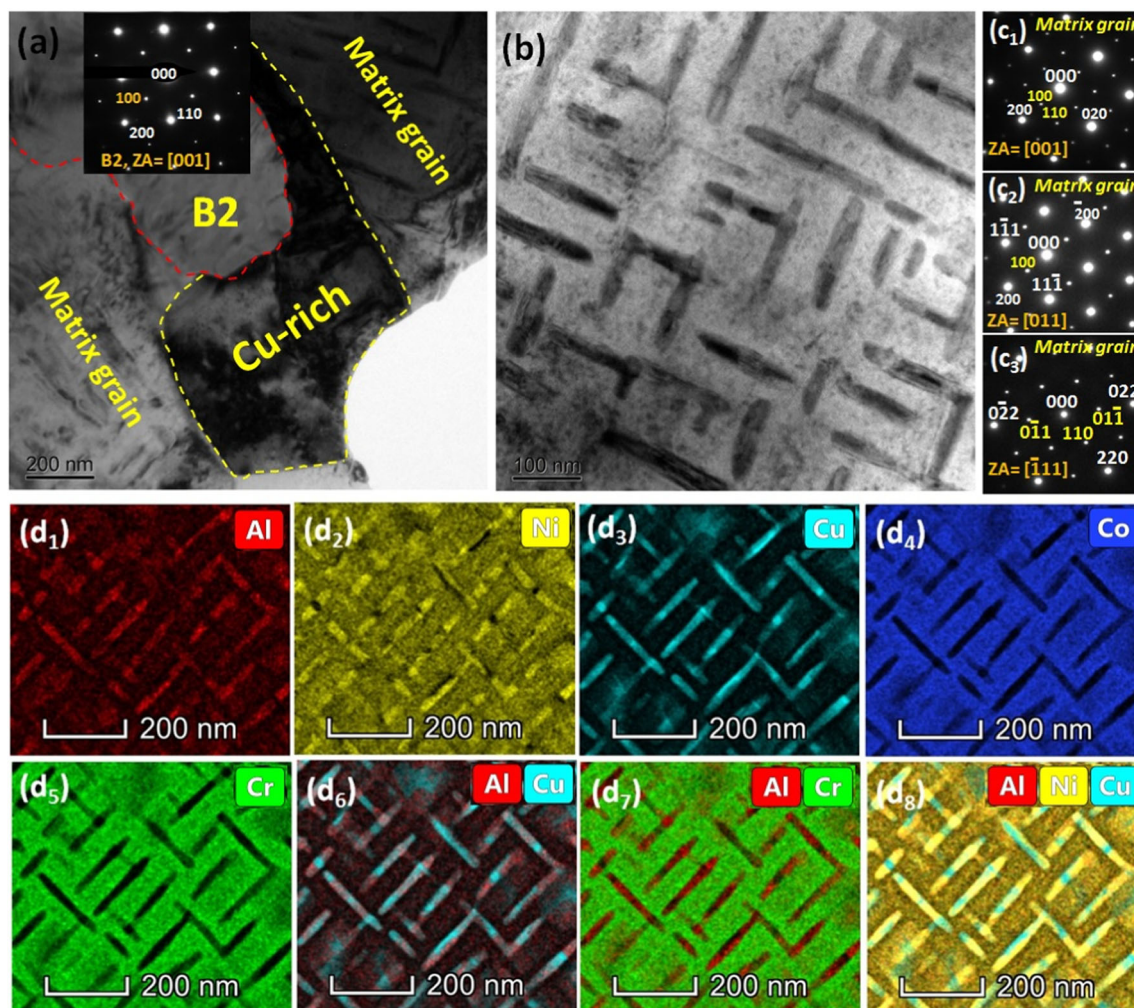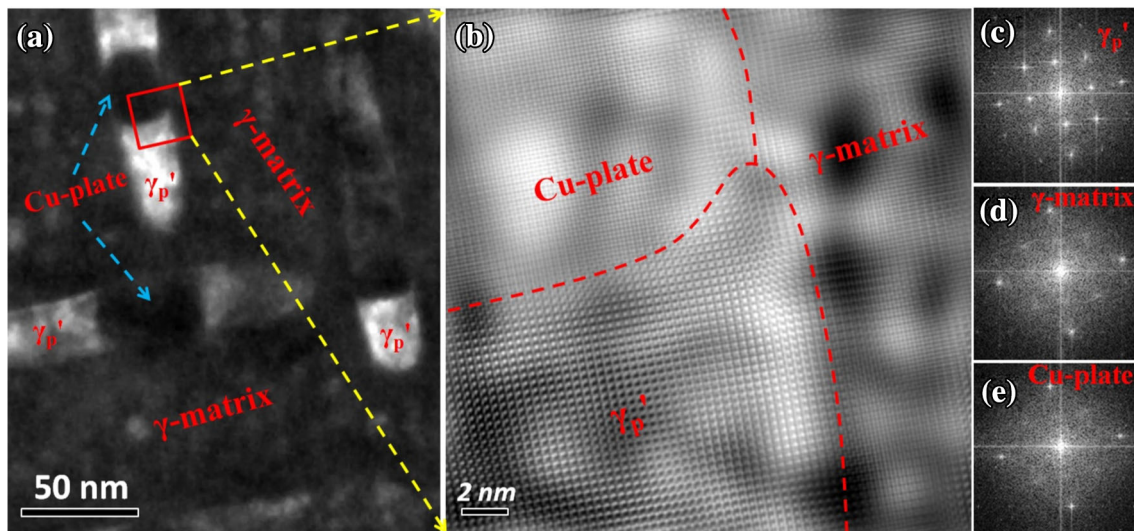
Figure 5 TEM characterization of the SPS-ed sample. **a** BF TEM image containing both the matrix grain and intergranular region. Inset shows the SADP along the [001] zone axis of the B2 phase. **b** BF TEM image of the matrix grain. **c₁–c₃** SADPs along the < 001 > , < 011 > and < 111 > zone axes of the matrix grain, respectively. **d₁–d₈** STEM-EDS elemental distribution maps along the < 001 > zone axis of various elements, as labeled in the image.

disordered FCC structure. In the BF TEM image of the dendritic matrix phase shown in Fig. 8d, a STEM-EDS compositional profile along the green arrow reveals a high amplitude fluctuation of the Cu element. The STEM-EDS elemental maps of the dendritic matrix shown in Fig. 8e–j, clearly reveal that the Cu-rich precipitates with several nanometers are dispersed in the matrix. This indicates the presence of microscopic Cu segregation within the dendritic matrix. Furthermore, it can be deduced that both the Cu-rich precipitates and the matrix possess the same disordered FCC structure because no additional spots or superlattice reflections are observed in either SADP (Fig. 8b or 8c).

SADPs along two different zone axes (< 013 > and < 112 >), which correspond to the interdendritic Cu-rich phase, are displayed in the insets of Fig. 9a. The main diffraction spots confirm that the matrix has an FCC structure, and the presence of faint superlattice reflections at the {001} or {011} positions indicates the existence of the $L1_2$ ordered structure inside the interdendritic Cu-rich phase. The DF TEM image (Fig. 9a) made from the {001} superlattice spot reveals that the fine nanoprecipitates with bright contrast are dispersed in the matrix. The HRTEM image in Fig. 9b, obtained from the square area in Fig. 9a, reveals that the precipitates possessing an ordered $L1_2$ structure with a mean size of approximately 2 nm are coherent with the

Figure 6 TEM characterization of the plate-like precipitate. **a** DF TEM image made from the {100} superlattice spot in the SADP of Fig. 5c$_1$. **b** HRTEM image corresponding the area indicated by the red box containing the γ matrix, Cu-plate and γ_p'. **c–e** Electron diffraction patterns of the γ_p', γ matrix, and Cu-plate, respectively, from FFT of (**b**).

disordered matrix. In addition, dislocations and lattice distortions are also observed in the HRTEM image. Note that the chemical compositions of both the L1$_2$ precipitates inside the interdendritic Cu-rich phase and the Cu-rich precipitates within the dendritic matrix have not been obtained due to their very small sizes.

Compressive properties

Figure 10 shows the compressive engineering stress–strain curves of both the SPS-ed and PTA remelted samples. Table 2 summarizes the experimental data of yield strength (σ_y) and fracture strain (ε_f) for both samples. After PTA remelting, the sample exhibits a lower yield strength but a much higher fracture strain than that of the SPS-ed sample. Note that the PTA remelted sample can be pressed into flat disk without fracture (compressive strain above 70%) and can still maintain an appreciable yield strength of 739.4 MPa, which indicates that an excellent balance between strength and ductility has been obtained after PTA remelting. However, the SPS-ed sample has only a compressive fracture strain of 21.7% despite a relative high yield strength of 913.8 MPa. The inferior ductility of the SPS-ed sample can be attributed to the coarse intragranular plate-like precipitates and the intergranular B2 phase, which leads to a brittle fracture. The related strengthening mechanisms for both

the SPS-ed and PTA remelted samples will be discussed in Sect. 4.2.

Corrosion properties

Figure 11a shows the potentiodynamic polarization curves of samples, both before and after PTA remelting. The polarization curve of the PTA remelted sample shifts to the upper left compared to that of the SPS-ed sample, which indicates a reduced polarized current density and an increased corrosion potential after PTA remelting. This can be substantiated by the electrochemical corrosion parameters extracted from the polarization curves, as listed in Table 3. The PTA remelted sample exhibits a nobler corrosion potential (E_{corr}) and a lower corrosion current density (i_{corr}) than those of the SPS-ed sample, which demonstrates an enhanced corrosion resistance after PTA remelting.

Figure 11b shows the Nyquist plots of both the SPS-ed and PTA remelted samples. Both of them are semicircular, indicating a mechanism of charge transfer. Generally, the larger the radius of the semicircle, the higher the corrosion resistance of the sample is. Thus, the Nyquist plots further substantiate that the PTA remelted sample has a better corrosion resistance than that of the SPS-ed sample, because the PTA remelted sample exhibits a larger radius of the semicircle. Combining the above
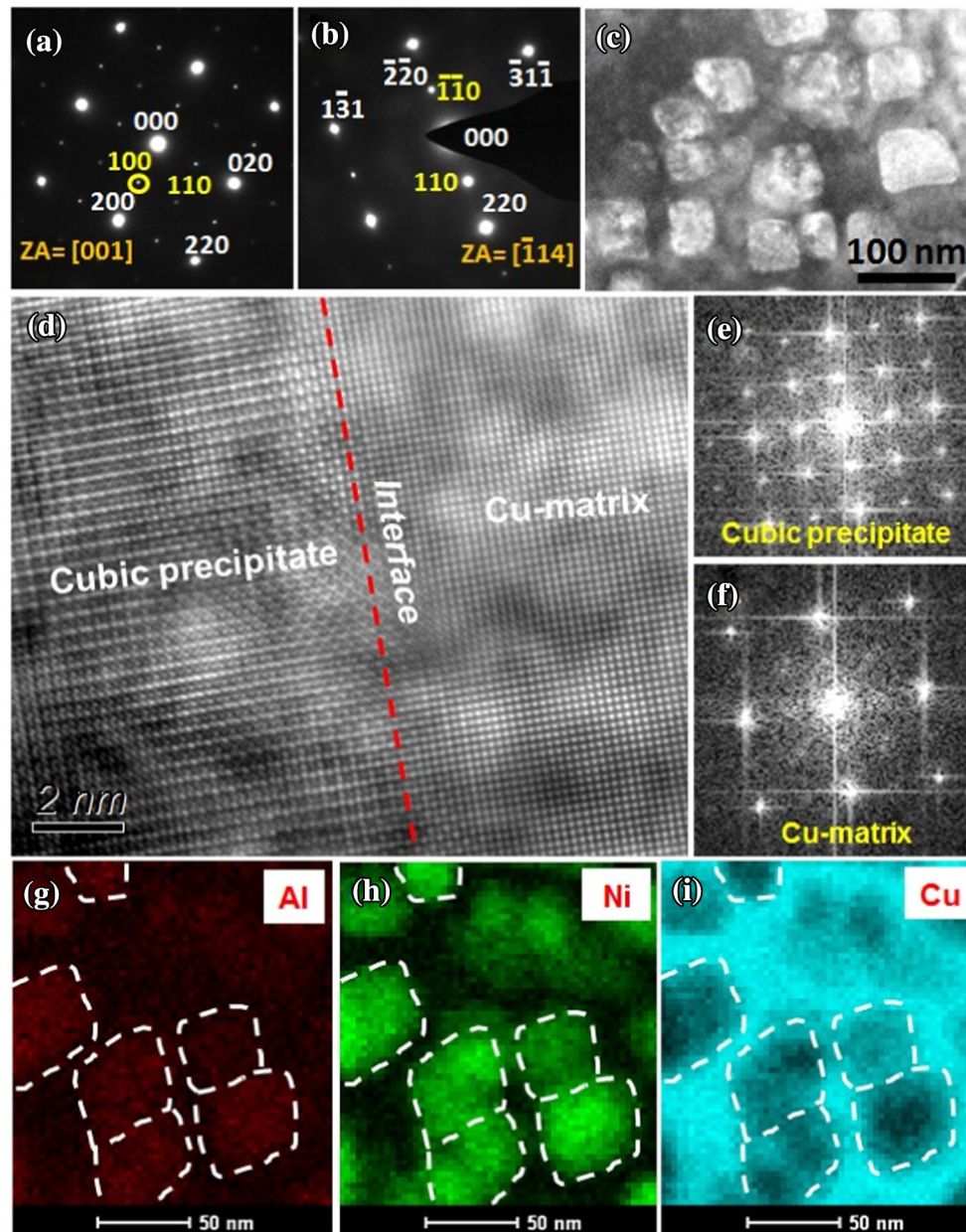
Figure 7 TEM characterization on the intergranular Cu-rich phase of the SPS-ed sample. **a, b** SADPs from the < 001 > and < 114 > zone axes of the Cu-rich phase, respectively. **c** DF TEM image made from the {100} superlattice spot in (**a**). **d** HRTEM image of the interface of matrix/cubic precipitate. **e, f** Electron diffraction patterns of the cubic precipitate and Cu-matrix, respectively, from FFT of (**d**). **g–i** STEM-EDS elemental distribution maps of the Cu-rich phase showing Al, Ni and Cu, respectively.

microstructure analyses, the enhanced corrosion resistance after PTA remelting can be attributed to the reduced elemental segregation, and the decreased sizes and types of the precipitated phases; thus, the galvanic corrosion tendency that is resulted from the multi-phase structures has been decreased.

Discussion

Microstructural evolution

The above analyses indicate that PTA remelting greatly affects the microstructures of SPS-ed CoCrCuNiAl$_{0.5}$ HEA. Understanding the microstructural evolution before and after PTA
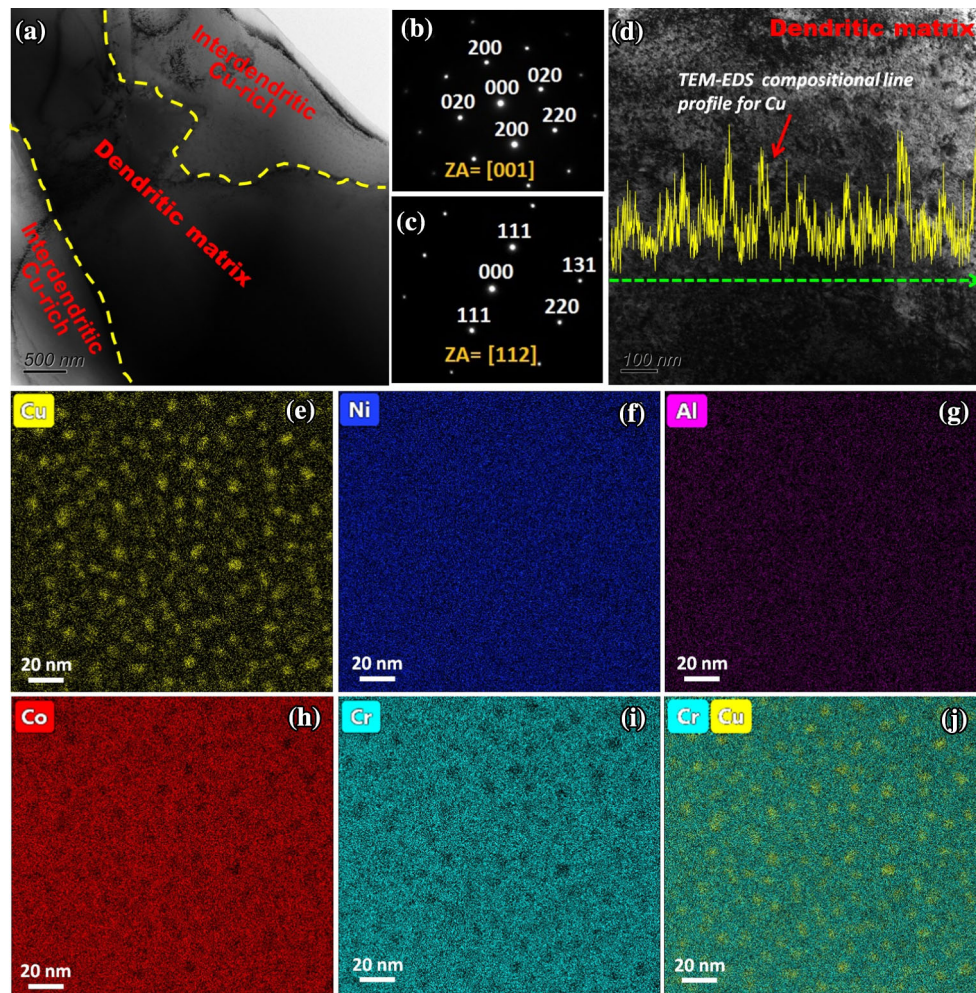
Figure 8 TEM characterization of the PTA remelted sample. **a** BF TEM image containing both the dendritic matrix and interdendritic regions. **b, c** SADPs from the < 001 > and < 112 > zone axes of the dendritic matrix, respectively. **d** BF TEM image of the dendritic matrix. Inset shows the STEM-EDS compositional profile of Cu along the green arrow. **e–j** STEM-EDS elemental distribution maps of various elements, as labeled in the image.

remelting is important to further control the microstructures and macroscopic mechanical properties of HEAs. Based on the microstructural characterization of both the SPS-ed and PTA remelted samples, the microstructural evolution was proposed, as shown in Fig. 12.

With regard to the HEA systems containing Cu element, obtaining the single-phase solid solution is difficult owing to the large positive mixing enthalpy between Cu and other elements [44]. Despite such HEA systems were successively rolled, annealed at high temperatures, and then water quenched, the microsegregation of Cu cannot be eliminated [45]. Some recent reports have also indicated that there is no single, stable, solid-state phase field in the HEA systems containing Cu between 1000 °C and the

solidus temperature because the enthalpic terms dominate the behavior of such HEAs; thus, these HEAs exist as two disordered FCC solid solution phases within this temperature range, i.e., the Cu-depleted matrix phase and the Cu-rich interdendritic phase [46, 47].

In this study, the SPS temperature of CoCrCuNiAl$_{0.5}$ HEA system is 1050 °C, which is between 1000 °C and its solidus temperature; thus, it can be deduced that two solid solutions, i.e., the matrix and intergranular Cu-rich phases, exist in equilibrium at high temperatures (Fig. 12a). This leads to a reduction in the entopic stabilization of solid solution phases and increases their susceptibility to phase decomposition at lower temperatures [46, 48], which is consistent with the microstructural
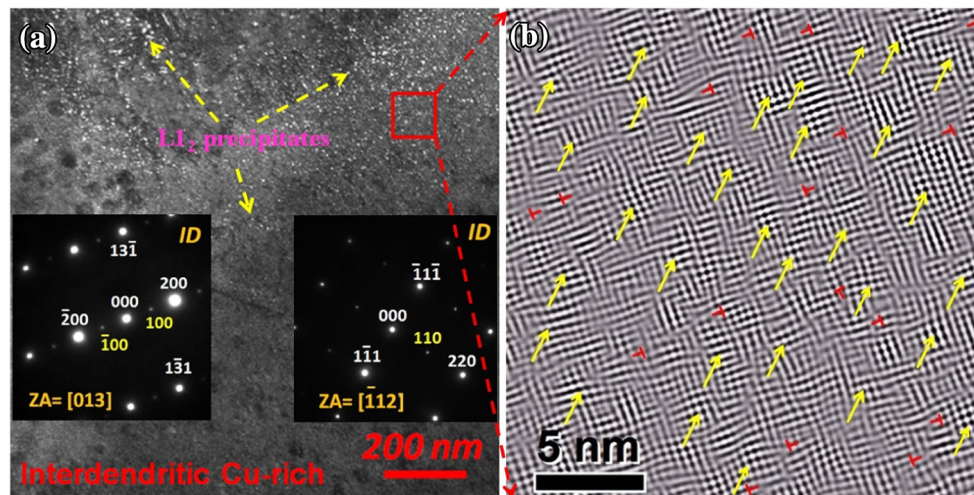
Figure 9 TEM characterization on the interdendritic Cu-rich phase of the PTA remelted sample. **a** DF TEM image made from the {001} superlattice spot showing the fine-scale precipitates dispersed in the Cu-rich phase. Inset shows SADPs along the < 013 > and < 112 > zone axes of the interdendritic Cu-rich phase shown as insets and correspondingly labeled. **b** HRTEM image corresponding the area indicated by the red box in (**a**) containing the matrix and fine-scale precipitates. "T" and arrows indicate dislocations and precipitates, respectively.
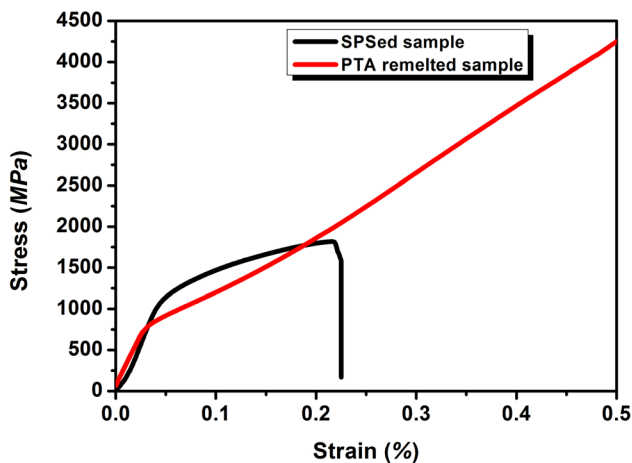
Figure 10 Representative engineering stress–strain curves of the SPS-ed and PTA remelted samples in compression.

Table 2 Compressive yield strength (σ_y) and fracture strain (ε_f) of the SPS-ed and PTA remelted samples at room temperature

Alloys	Yield strength (σ_y) (MPa)	Fracture strain (ε_f) (%)
SPS-ed sample	913.8	21.7
PTA remelted sample	739.4	> 70 (without fracture)

observations containing the various disordered and ordered phases in the sample after SPS. With the decrease in temperature after SPS, the portion of Cu that is retained in the matrix solid solution at high temperatures is repelled from the γ matrix due to mixing enthalpy to form a disordered FCC Cu-rich plate-like phase (further termed as γ_{Cu}) inside the matrix grains via spinodal decomposition [6, 49], as shown in Fig. 12b. Then, phase separation in γ_{Cu} results in the formation of disordered FCC Cu-plate and ordered γ_p' (Fig. 12c). The phase separation can also be verified by the Ni–Al–Cu ternary phase diagram [50] and our previous report on the $Co_{25}Cr_{25}Cu_{12.5}Ni_{25}Al_{12.5}$ HEA [6]. The formation of L1$_2$ cubic precipitates inside the intergranular Cu-rich phase can be ascribed to the process of precipitation and growth during cooling (Fig. 12d). Such behavior is similar to the metallurgy of Ni-base super alloys, in which the solid-state precipitation of the γ′ phase occurs during cooling, forming the typical γ + γ′ microstructures [51, 52]. In addition, the Ni–Al-rich ordered B2 phase is also observed between the matrix grain and the intergranular Cu-rich phase, primarily due to the large negative mixing enthalpy between Ni and Al (−22 kJ mol^{-1}) [44].

After the SPS-ed sample was remelted by PTA (Fig. 12e), nucleation and growth occur (Fig. 12f). The PTA remelted sample exhibits a directional solidified morphology with specific growth orientations (Fig. 12g). This can be ascribed to the ultrahigh temperature gradient produced by non-equilibrium plasma beam heating, which results in the preferential growth of the FCC solid solution along its low-
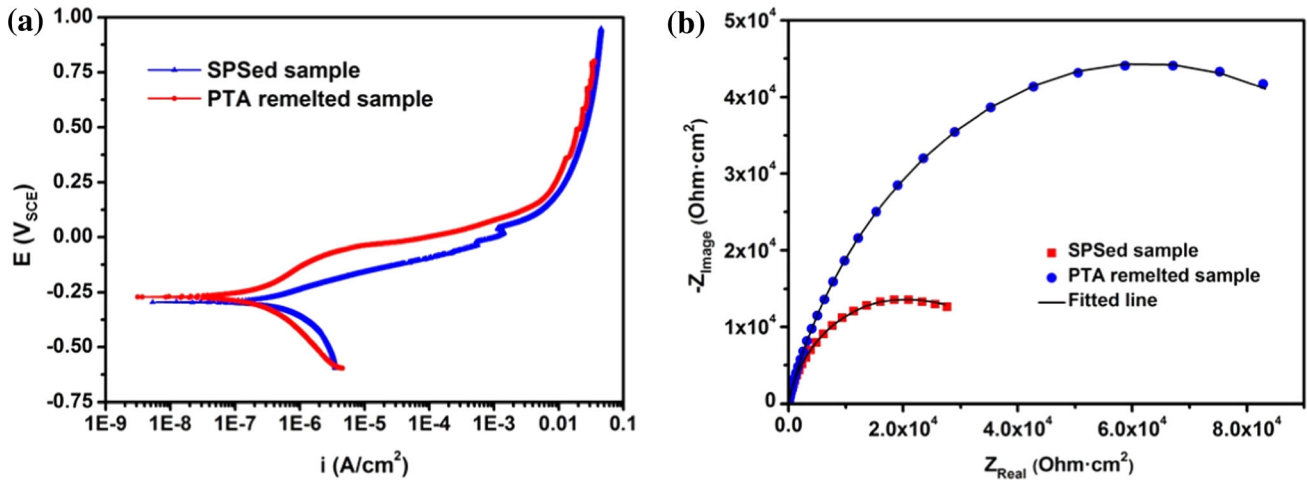
Figure 11 Electrochemical test results of the SPS-ed and PTA remelted samples. **a** Potentiodynamic polarization curves. **b** Nyquist plots.

Table 3 Potentiodynamic polarization parameters of the SPS-ed and PTA remelted samples in the 3.5 wt% NaCl solution at room temperature

Alloys	E_{corr} (mV/SCE)	i_{corr} (μA/cm²)
PTA remelted sample	−271.2	3.11×10^{-2}
SPS-ed sample	−296.0	1.05×10^{-1}

index planes. Evidently, the coarse B2 phase has disappeared after PTA remelting. The B2 phase has a solvus temperature of approximately 975 °C and can form after 0.1 h of exposure at 800–900 °C and after 1 h at 700 °C in the intergranular region, while it needs 50 h of exposure at 700 °C inside the matrix grain [53]. Hence, the slow cooling rates after SPS can easily result in the formation and growth of the B2 phase in the intergranular region. While for the PTA remelting process, the rapid cooling rate can restrict the formation and growth of the B2 phase. Compared with the intricate ordered L1₂ and disordered FCC phases inside the matrix grains in the SPS-ed sample, the PTA remelted sample only contains the disordered FCC fine-scale Cu-rich precipitates in its dendritic matrix (Fig. 12h), which are also attributed to the rapid cooling rate during PTA remelting that leads to the formation of a non-equilibrium phase. This also suggests that it is difficult to eliminate microscopic Cu segregation. Combining the evolution analysis of the γ_{Cu} phase in the SPS-ed sample, the formation of Cu-rich precipitates inside the dendritic matrix is deduced to result from the rapid spinodal decomposition. For the SPS-ed sample, the lower cooling rates can facilitate the spinodal

decomposition, and the phase size resulted from spinodal decomposition increases with the decrease of cooling rates [6]; thus, the Cu-rich precipitates have developed into coarse plate-like shapes in the SPS-ed sample. However, in the case of PTA remelted sample, the rapid cooling rate produces a "rapid quenching" effect [54] that can restrict the diffusion of the elements during spinodal decomposition and result in the formation of metastable Cu-rich precipitates with the size of several nanometers.

The sizes of the L1₂ precipitates inside the intergranular Cu-rich phase are decreased from ∼ 55 nm in the SPS-ed sample to ∼ 2 nm after PTA remelting, which indicates that PTA remelting refines the nanoprecipitates effectively. The presence of dislocations and lattice distortions in the HRTEM image of the interdendritic Cu-rich phase (Fig. 9b) can be explained as follows. In the HEAs containing multiple principal elements, the increased lattice distortion induced by the interaction of various elements with different atomic radii results in the formation of a high density of dislocations in the solid solutions. This is especially noted during rapid cooling, which can further restrict the elemental diffusion and is more conducive to the formation of the HEA supersaturated solid solutions [55, 56].

Strengthening mechanisms

As indicated in Sect. 3.3, the SPS-ed and PTA remelted samples exhibit the yield strengths of 913.8 and 739.4 MPa, respectively. The change in yield
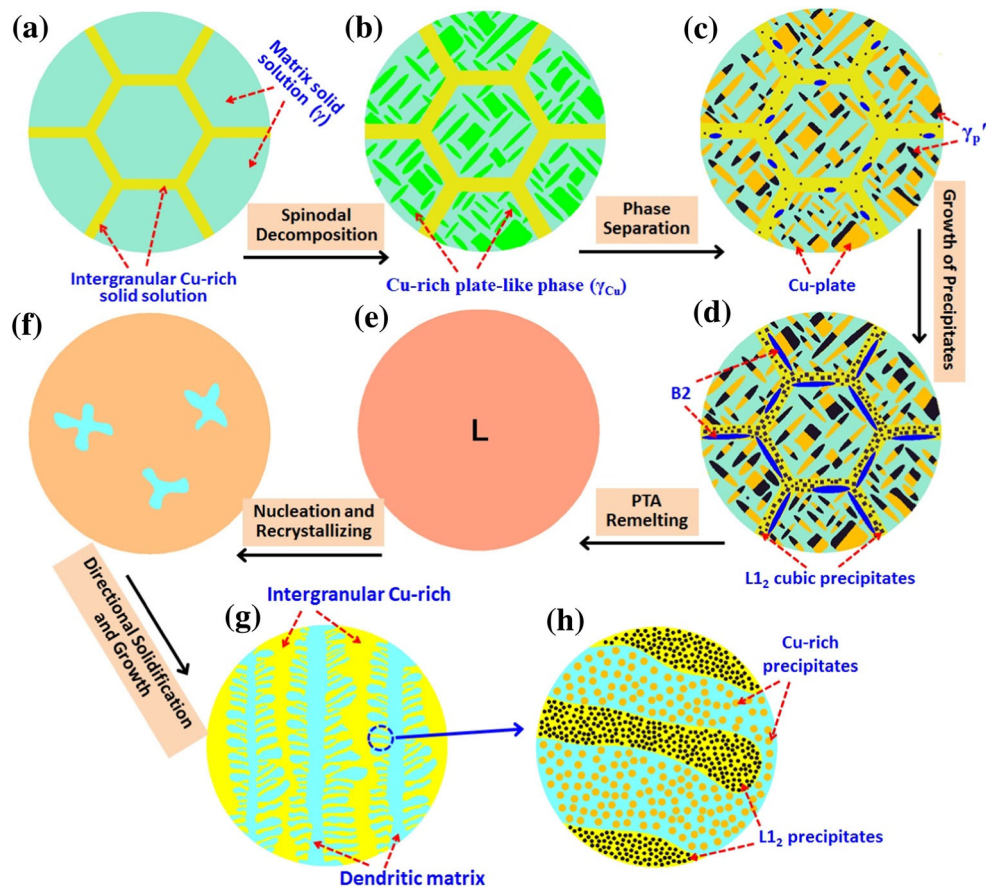
Figure 12 The proposed schematic representation of the microstructural evolution. **a** Formation of the FCC matrix and intergranular Cu-rich solid solutions at high temperatures during SPS. **b** Formation of the Cu-rich plate-like phases (γ_{Cu}) inside the FCC matrix via spinodal decomposition with the temperature decreasing after SPS. **c** Formation of the γ_p' and Cu-plate via phase separation in γ_{Cu}, and nucleation of the $L1_2$ cubic precipitates in the intergranular Cu-rich phase, as well as the formation B2 phase between the matrix grain and intergranular Cu-rich phase.

d Growth of the γ_p', $L1_2$ cubic precipitates and B2 phase. **e** Formation of molten state during PTA remelting. **f** Occurrence of nucleation and recrystallization after PTA remelting. **g** Formation of directional solidified morphology with the temperature decreasing. **h** The magnified image corresponding the area indicated by blue circle in (**g**) showing the Cu-rich precipitates dispersed in the dendritic matrix and $L1_2$ precipitates dispersed in the interdendritic region.

strength after PTA remelting could be related to different strengthening mechanisms. Both the samples are polycrystalline materials, and the yield strength (σ_y) from various strengthening contributions can be expressed as [57, 58]:

$$\sigma_y = \sigma_0 + \Delta\sigma_{ss} + \Delta\sigma_{gb} + \Delta\sigma_{dis} + \Delta\sigma_p \qquad (1)$$

where σ_0 is the intrinsic lattice frictional stress, and $\Delta\sigma_{ss}$, $\Delta\sigma_{gb}$, $\Delta\sigma_{dis}$, and $\Delta\sigma_p$ are strengthening contributions from solid solution, grain boundary, dislocations, and precipitates, respectively. σ_0 is estimated to be approximately 115 MPa for both samples by using the rule of mixtures [58, 59].

The evaluation of $\Delta\sigma_{ss}$ in traditional approaches is usually based on dilute solid solutions, which may not be valid for HEAs because they are considered to be highly concentrated. However, for the current Al–Cr–Cu–Co–Ni system, the lattice strain is mainly caused by Al due to its larger atomic radius (r_{Al} = 0.143 nm) than other alloying elements. Thus, CrCuCoNi and Al can be simply treated as the solvent and the solute, respectively. A model based on elastic dislocation–solute interactions can be used to evaluate the solid-solution strengthening [57, 60]:

$$\Delta\sigma_{ss} = M \cdot \frac{G \cdot \varepsilon_s^{3/2} c^{1/2}}{700} \tag{2}$$

where M is the Taylor factor with a value of 3.06, which indicates the conversion of shear stress to normal stress for an FCC polycrystalline matrix. G (shear modulus) is calculated to be ~ 74 GPa [6]. c is the total molar ratio of Al in the FCC matrix. ε_s is the interaction parameter and can be expressed as [57]:

$$\varepsilon_s = \left| \frac{\varepsilon_G}{1 + 0.5\varepsilon_G} - 3 \cdot \varepsilon_a \right| \tag{3}$$

where ε_G and ε_a are elastic and atomic size mismatches, respectively, and they can be separately defined as $\varepsilon_s = \frac{1}{G}\frac{\partial G}{\partial c}$ and $\varepsilon_a = \frac{1}{G}\frac{\partial a}{\partial c}$, in which a is the lattice parameter of the FCC matrix. The a values for the SPS-ed and PTA remelted samples are 0.3596 and 0.3703 nm, respectively, based on the XRD results. Therefore, with these parameters, the strength contributions from solid-solution strengthening ($\Delta\sigma_{ss}$) are estimated to be approximately 27 and 34 MPa, respectively. The higher solid-solution strengthening contribution in PTA remelted sample than that of the SPS-ed sample can be ascribed to the increased solid solubility of elements, especially Al, consistent with the EDS results as indicated in Sect. 3.1.

Contribution from grain boundary can be well described by the traditional Hall–Petch theory. The relationship between yield strength and grain size can be expressed as [57, 61]:

$$\Delta\sigma_{gb} = K^{HP}d^{-1/2} \tag{4}$$

where K^{HP} is the Hall–Petch coefficient with an estimated value of ~ 0.6 MPa m$^{-1/2}$ for coarse-grained FCC-based HEAs [61, 62] and d is the average grain size of the sample. As shown in Fig. 4a, the SPS-ed sample exhibits an equiaxed polygonal grain structure, and its average grain size was calculated to be ~ 11.2 μm from the orientation imaging microscopy scan using the equivalent diameter method. After PTA remelting, the sample microstructure was transformed into a dendritic one, and the average size of secondary dendritic arm spacing was carefully analyzed by using the ImageJ software. >5 BSE images were used and averaged, and the obtained result was ~ 3.4 μm. Thus, the calculated values of $\Delta\sigma_{gb}$ for the SPS-ed and PTA remelted samples are ~ 179 and ~ 325 MPa, respectively.

Dislocation strengthening ($\Delta\sigma_{dis}$) is resulted from the interaction of dislocations during deformation.

Generally, a higher dislocation density leads to a higher yield strength. A Bailey-Hirsch formula [57, 61] is used to calculate the $\Delta\sigma_{dis}$ and can be expressed as:

$$\Delta\sigma_{dis} = M\alpha Gb\rho^{1/2} \tag{5}$$

where α is 0.2 for FCC metals, which represents a correction factor. b is the Burgers vector, and can be calculated as $b = \frac{\sqrt{2}}{2}a$, in which a is the lattice parameter for the FCC matrix; thus, the b values for the SPS-ed and PTA remelted samples are determined to be 0.2543 and 0.2618 nm, respectively. ρ is the dislocation density and can be calculated as [57, 61]:

$$\rho = \frac{2\sqrt{3}\varepsilon}{Db} \tag{6}$$

where ε and D are the micro-strain and crystallite size, both of which are calculated from the XRD patterns by using the Williamson–Hall method [63]. In the XRD pattern, the true XRD peak broadening B consists of crystallite size broadening and microstrain broadening, and the relation among B, D and ε can be defined as: $B\cos\theta = \frac{K\lambda}{D} + (4\sin\theta)\varepsilon$ [57, 63], in which θ is the Bragg angle of the certain peak, $\lambda = 0.15405$ nm is the wavelength of Cu Kα radiation, and K is a constant with a value of ~ 0.9. The parameter ε can be determined from the slope of the linear fit of the $B\cos\theta$–$4\sin\theta$ Hence, with these parameters, the ρ values for the SPS-ed and PTA remelted samples are determined to be 5.9×10^{13} m^{-2} and 3.6×10^{14} m^{-2}, respectively. From Eq. (5), the strengthening contributions from dislocation are evaluated as 88.4 MPa and 224.9 MPa for the SPS-ed and PTA remelted samples, respectively. Compared with the SPS-ed sample, the strengthening contribution from dislocation in the PTA remelted sample is much higher. This can be attributed to the rapid cooling rate during PTA remelting, which results in the formation of a high density of dislocations due to the extended solid solubility and hence the increased lattice distortion.

As indicated in the above microstructural observations, both the SPS-ed and PTA remelted samples contain matrix grains and intergranular Cu-rich regions. A composite model can be used to evaluate the precipitation strengthening ($\Delta\sigma_p$) [57]:

$$\Delta\sigma_p = \Delta\sigma_m \cdot f_m + \Delta\sigma_i \cdot f_i \tag{7}$$

where $\Delta\sigma_m$ and $\Delta\sigma_i$ are the precipitation strengthening from the matrix grains and intergranular Cu-

rich regions, respectively; f_m and f_i represent the volume fractions of the matrix grains and intergranular Cu-rich regions, respectively, which are analyzed by the ImageJ software. Quantitative analysis of the BSE images shows that the f_m and f_i in the SPS-ed sample are 78.83% and 16.09%, respectively. The f_m and f_i of the PTA remelted sample are 89.42% and 10.58%, respectively. For the SPS-ed sample, the precipitates inside the matrix grains are plate-like, a modified Orowan–Ashby equation can be used to calculate the precipitation strengthening caused by the plate-like precipitates ($\Delta\sigma_m$) [64]:

$$\Delta\sigma_m = \frac{Gb}{2\pi\sqrt{1-\upsilon}}\left(\frac{1}{1.145\sqrt{\frac{0.306\pi d_p t}{f}} - \left(\frac{\pi d_p}{8}\right) - 1.061t}\right)\ln\frac{0.981\sqrt{d_p t}}{b}$$

(8)

where d_p, t and f are the mean diameter, the mean thickness and volume fraction of the plate-like precipitates, respectively. The d_p, t and f are analyzed by using the ImageJ software, and obtained results are approximately 128.9 nm, 16.9 nm, and 26.7%, respectively. υ is Poisson's ratio with a value of 0.33. Thus, the $\Delta\sigma_m$ is determined to be 578.6 MPa via Eq. (8).

The L1$_2$ cubic precipitates inside the intergranular Cu-rich region have a similar size with the plate-like precipitates; thus, the strengthening contribution produced by the cubic precipitates ($\Delta\sigma_i$) can also be evaluated using the modified Orowan–Ashby model by treating the cubic precipitates as the plate-like inclusions of $d_c = t_c$ (d_c and t_c represent the mean diameter and thickness of the cubic precipitates). By using the same method, the $\Delta\sigma_i$ is estimated as 397.5 MPa. Therefore, the $\Delta\sigma_p$ was determined to be 520.1 MPa from Eq. (7).

The precipitation strengthening would be dominated by the particle shearing mechanism when the precipitates are sufficiently small and coherent [57, 65]. Both the precipitates within the dendritic matrix and inside the interdendritic Cu-rich phase are several nanometers in the PTA remelted sample; furthermore, both types of precipitates are coherent with their matrix. Hence, a particle shearing model [57, 66] is used to estimate the precipitation strengthening in the PTA remelted sample. Three contributing factors should be considered for the shearing mechanism [65, 67], which can be expressed as follows:

$$\Delta\sigma_{cs} = M \cdot \alpha_\varepsilon (G \cdot \varepsilon_c)^{3/2} \left(\frac{d_s f_s}{Gb}\right)^{1/2}$$

(9)

$$\Delta\sigma_{ms} = M \cdot 0.0055 \cdot (\Delta G)^{\frac{3}{2}} \left(\frac{2f_s}{G}\right)^{1/2} \left(\frac{d_s}{2b}\right)^{\frac{3m}{2}-1}$$

(10)

$$\Delta\sigma_{os} = M \cdot 0.81 \cdot \frac{\gamma_{apb}}{2b} \left(\frac{3\pi f_s}{8}\right)^{1/2}$$

(11)

where $\Delta\sigma_{cs}$, $\Delta\sigma_{ms}$ and $\Delta\sigma_{os}$ are coherency strengthening, modulus mismatch strengthening and order strengthening, respectively. $\Delta\sigma_{cs}$ and $\Delta\sigma_{ms}$ play the role prior to the shearing, while $\Delta\sigma_{os}$ works during the shearing. Thus, the larger contribution of $\Delta\sigma_{cs} + \Delta\sigma_{ms}$ or $\Delta\sigma_{os}$ determines the strengthening contribution from the nanoprecipitates. α_ε is a constant with a value of 2.6 for the FCC structure, and ε_c is the constrained lattice parameter mismatch and can be calculated as $\varepsilon_c \approx \frac{2}{3}\left(\frac{\Delta a}{a}\right)$, in which Δa is the difference of the lattice parameter between the nanoprecipitate and matrix. d_s and f_s are the average diameter and the volume fraction of the nanoprecipitates, respectively, which are analyzed by the ImageJ software. The values of d_s are determined to be $\sim$ 5 nm and $\sim$ 2 nm within the dendritic matrix and inside the interdendritic Cu-rich region, respectively. The corresponding values of f_s are $\sim$ 8.2% and $\sim$ 10.4%, respectively. ΔG is the mismatch of shear modulus between the nanoprecipitate and matrix. m is a constant with a value of 0.85, and γ_{apb} is the anti-phase boundary free energy. The values of ΔG and γ_{apb} are determined as 4 GPa and 0.12 J/m^2 [68], respectively. The nanoprecipitates inside the dendritic matrix have a disordered FCC structure; and thus only the $\Delta\sigma_{cs}$ is considered. With the related parameters, the calculated value of $\Delta\sigma_{cs}$ is 104.8 MPa. For the interdendritic Cu-rich region, the nanoprecipitates have an ordered L1$_2$ structure; and thus, the above three strengthening contributions should be considered. The calculated values of $\Delta\sigma_{cs}$, $\Delta\sigma_{ms}$ and $\Delta\sigma_{os}$ for the interdendritic Cu-rich region are 424.9 MPa, 10.3 MPa and 198.6 MPa, respectively. The value of $\Delta\sigma_{cs} + \Delta\sigma_{ms}$ (435.2 MPa) is much larger than that of the $\Delta\sigma_{os}$ (198.6 MPa). Thus, the $\Delta\sigma_{cs} + \Delta\sigma_{ms}$ determines the resultant contribution in the interdendritic Cu-rich region. Consequently, the $\Delta\sigma_p$ is determined to be 139.7 MPa from Eq. (7).

Based on Eq. (1), the values of σ_y for the SPS-ed and PTA remelted samples are calculated as 929.5 and 838.6 MPa, respectively, both of which are

somewhat higher than that of the respective experimental results. However, the agreement between the calculated and experimental values is acceptable. For the SPS-ed sample, the precipitation strengthening offers the largest strength increment (520.1 MPa), but the coarse precipitates lead to the brittle fracture. While for the PTA remelted sample, the grain boundary strengthening offers the largest strength increment (325 MPa), followed by dislocation strengthening (224.9 MPa). These two strengthening mechanisms tremendously increase the strength of the PTA remelted sample and do not result in the brittle failure. Therefore, an excellent balance between strength and ductility has been obtained after the PTA remelting treatment.

Conclusion

The CoCrCuNiAl$_{0.5}$ HEA was prepared by SPS and subsequently was performed by PTA remelting. The microstructures and properties of both the SPS-ed and PTA remelted samples were investigated and compared. The following conclusions were reached:

(1) The microstructures transformed from an equiaxed structure in the SPS-ed sample to a dendritic structure with a directional solidified morphology after PTA remelting under the effect of ultrahigh temperature gradient produced by non-equilibrium plasma beam.

(2) After PTA remelting, the coarse plate-like precipitates with $\sim$ 130 nm in diameter and $\sim$ 20 nm in thickness containing ordered L1$_2$ and disordered FCC structures were replaced by the disordered FCC spherical Cu-rich precipitates with several nanometers in the intragranular region. In the intergranular region, the brittle B2 phase was disappeared, and the extent of Cu segregation was decreased. Furthermore, the size of the L1$_2$ cubic precipitates was decreased from $\sim$ 55 nm to $\sim$ 2 nm, and dislocations and lattice distortions were observed.

(3) The SPS-ed sample has a compressive yield strength of 913.8 MPa and a fracture strain of 21.7%. After PTA remelting, the sample exhibits a much higher fracture strain ($>$ 70%, without fracture) and an appreciable yield strength of 739.4 MPa, which indicates an excellent balance between strength and ductility was achieved. The quantitative

contributions from each strengthening mechanism were estimated using available strengthening theories. Grain boundary strengthening and dislocation strengthening are principally responsible for the measured yield strength of the PTA remelted sample. Precipitation strengthening offers the largest strength increment for the SPS-ed sample, but the coarse precipitates leads to a brittle fracture.

(4) The PTA remelted sample exhibits the nobler corrosion potential (E_{corr}) and the lower corrosion current density (i_{corr}) than that of the SPS-ed sample. This indicates the enhanced corrosion resistance after PTA remelting due to the decreased elemental segregation, and the reduced sizes and types of the precipitates.

Availability of data

The raw/processed data required to reproduce these findings cannot be shared at this time as the data also forms part of an ongoing study.

Compliance with ethical standards

Conflict of interest The authors declare that they have no known competing financial interests or personal relationships that could have appeared to influence the work reported in this paper.

References

[1] Yeh JW, Chen SK, Lin SJ, Gan JY, Chin TS, Shun TT, Tsau CH, Chang SY (2004) Nanostructured high-entropy alloys with multiple principal elements: novel alloy design concepts and outcomes. Adv Eng Mater 6:299–303

[2] Guo Z, Zhang A, Han J, Meng J (2019) Effect of Si additions on microstructure and mechanical properties of refractory NbTaWMo high-entropy alloys. J Mater Sci 54:5844–5851. https://doi.org/10.1007/s10853-018-03280-z

[3] Fu Z, Jiang L, Wardini JL, MacDonald BE, Wen H, Xiong W, Zhang D, Zhou Y, Rupert TJ, Chen W, Lavernia EJ (2018) A high-entropy alloy with hierarchical nanoprecipitates and ultrahigh strength. Sci Adv 4(10):8712s

[4] Ding Q, Zhang Y, Chen X, Fu X, Chen D, Chen S, Gu L, Wei F, Bei H, Gao Y, Wen M, Li J, Zhang Z, Zhu T, Ritchie RO, Yu Q (2019) Tuning element distribution, structure and properties by composition in high-entropy alloys. Nature 574(7777):223

[5] Qiu X (2018) Microstructure, hardness and corrosion resistance of Al$_2$CoCrCuFeNiTix high-entropy alloy coatings prepared by rapid solidification. J Alloys Compd 735:359–364

[6] Wang M, Cui H, Zhao Y, Wang C, Wei N, Zhao Y, Zhang X, Song Q (2019) A simple strategy for fabrication of an FCC-based complex concentrated alloy coating with hierarchical nanoprecipitates and enhanced mechanical properties. Mater Des 180:107893

[7] Gludovatz B, Hohenwarter A, Catoor D, Chang EH, George EP, Ritchie RO (2014) A fracture-resistant high-entropy alloy for cryogenic applications. Science 345(6201):1153–1158

[8] Huo W, Fang F, Liu X, Tan S, Xie Z, Jiang J (2019) Fatigue resistance of nanotwinned high-entropy alloy films. Mater Sci Eng A 739:26–30

[9] Tang Z, Yuan T, Tsai CW, Yeh JW, Lundin CD, Liaw PK (2015) Fatigue behavior of a wrought Al$_{0.5}$CoCrCuFeNi two-phase high-entropy alloy. Acta Mater 99:247–258

[10] Senkov ON, Scott JM, Senkova SV, Meisenkothen F, Miracle DB, Woodward CF (2012) Microstructure and elevated temperature properties of a refractory TaNbHfZrTi alloy. J Mater Sci 47:4062–4074. https://doi.org/10.1007/s10853-012-6260-2

[11] Lu Y, Dong Y, Jiang H, Wang Z, Cao Z, Guo S, Wang T, Li T, Liaw PK (2020) Promising properties and future trend of eutectic high entropy alloys. Scr Mater 187:202–209

[12] Wu YD, Cai YH, Wang T, Si JJ, Zhu J, Wang YD, Hui XD (2014) A refractory Hf$_{25}$Nb$_{25}$Ti$_{25}$Zr$_{25}$ high-entropy alloy with excellent structural stability and tensile properties. Mater Lett 130:277–280

[13] Ye YX, Liu CZ, Wang H, Nieh TG (2018) Friction and wear behavior of a single-phase equiatomic TiZrHfNb high-entropy alloy studied using a nanoscratch technique. Acta Mater 147:78–89

[14] Zhao Y, Cui H, Wang M, Zhao Y, Zhang X, Wang C (2018) The microstructures and properties changes induced by Al: Co ratios of the A$_l$XCrC$_{o_2}$-XFeNi high entropy alloys. Mater Sci Eng A 733:153–163

[15] Yu Y, He F, Qiao Z, Wang Z, Liu W, Yang J (2019) Effects of temperature and microstructure on the triblogical properties of CoCrFeNiNbx eutectic high entropy alloys. J Alloys Compd 775:1376–1385

[16] Qiu Y, Thomas S, Fabijanic D, Barlow AJ, Fraser HL, Birbilis N (2019) Microstructural evolution, electrochemical and corrosion properties of AlxCoCrFeNiTiy high entropy alloys. Mater Des 170:107698

[17] Dai C, Zhao T, Du C, Liu Z, Zhang D (2020) Effect of molybdenum content on the microstructure and corrosion behavior of FeCoCrNiMox high-entropy alloys. J Mater Sci Technol 46:64–73

[18] Torbati-Sarraf H, Shabani M, Jablonski PD, Pataky GJ, Poursaee A (2019) The influence of incorporation of Mn on the pitting corrosion performance of CrFeCoNi high entropy alloy at different temperatures. Mater Des 184:108170

[19] Zhao Y, Wang M, Cui H, Zhao Y, Song X, Zeng Y, Gao X, Lu F, Wang C, Song Q (2019) Effects of Ti-to-Al ratios on the phases, microstructures, mechanical properties, and corrosion resistance of Al$_{2-x}$CoCrFeNiTi$_x$ high-entropy alloys. J Alloys Compd 805:585–596

[20] Kulkarni R, Murty BS, Srinivas V (2018) Study of microstructure and magnetic properties of AlNiCo(CuFe) high entropy alloy. J Alloys Compd 746:194–199

[21] Feng XB, Zhang JY, Xia ZR, Fu W, Wu K, Liu G, Sun J (2018) Stable nanocrystalline NbMoTaW high entropy alloy thin films with excellent mechanical and electrical properties. Mater Lett 210:84–87

[22] Mishra RK, Shahi RR (2017) Phase evolution and magnetic characteristics of TiFeNiCr and TiFeNiCrM (M = Mn, Co) high entropy alloys. J Magn Magn Mater 442:218–223

[23] Lu C, Niu L, Chen N, Jin K, Yang T, Xiu P, Zhang Y, Gao F, Bei H, Shi S, He MR, Robertson IM, Weber WJ, Wang L (2016) Enhancing radiation tolerance by controlling defect mobility and migration pathways in multicomponent single-phase alloys. Nat Commun 7:13564

[24] El-Atwani O, Li N, Li M, Devaraj A, Baldwin JKS, Schneider MM, Sobieraj D, Wróbel JS, Nguyen-Manh D, Maloy SA, Martinez E (2019) Outstanding radiation resistance of tungsten-based high-entropy alloys. Sci Adv 5:2002

[25] Lu Y, Huang H, Gao X, Ren C, Gao J, Zhang H, Zheng S, Jin Q, Zhao Y, Lu C, Wang T, Li T (2019) A promising new

class of irradiation tolerant materials: $Ti_2ZrHfV_{0.5}Mo_{0.2}$ high-entropy alloy. J Mater Sci Technol 35:369–373

[26] Zhang A, Han J, Meng J, Su B, Li P (2016) Rapid preparation of AlCoCrFeNi high entropy alloy by spark plasma sintering from elemental powder mixture. Mater Lett 181:82–85

[27] Wang M, Cui H, Zhao Y, Wang C, Wei N, Gao X, Song Q (2019) Enhanced strength and ductility in a spark plasma sintered $CoCrCu_{0.5}NiAl_{0.5}$ high-entropy alloy via a double-step ball milling approach for processing powders. Mater Sci Eng A 762:138071

[28] Shi P, Ren W, Zheng T, Ren Z, Hou X, Peng J, Hu P, Gao Y, Zhong Y, Liaw PK (2019) Enhanced strength–ductility synergy in ultrafine-grained eutectic high-entropy alloys by inheriting microstructural lamellae. Nat Commun 10:489

[29] Reddy SR, Yoshida S, Bhattacharjee T, Sake N, Lozinko A, Guo S, Bhattacharjee PP, Tsuji N (2019) Nanostructuring with structural-compositional dual heterogeneities enhances strength-ductility synergy in eutectic high entropy alloy. Sci Rep 9:11505

[30] Reddy SR, Sunkari U, Lozinko A, Saha R, Guo S, Bhattacharjee PP (2019) Microstructural design by severe warm-rolling for tuning mechanical properties of $AlCoCrFeNi_{2.1}$ eutectic high entropy alloy. Intermetallics 114:106601

[31] Schuh B, Mendez-Martin F, Völker B, George EP, Clemens H, Pippan R, Hohenwarter A (2015) Mechanical properties, microstructure and thermal stability of a nanocrystalline CoCrFeMnNi high-entropy alloy after severe plastic deformation. Acta Mater 96:258–268

[32] Tang QH, Huang Y, Huang YY, Liao XZ, Langdon TG, Dai PQ (2015) Hardening of an $Al_{0.3}CoCrFeNi$ high entropy alloy via high-pressure torsion and thermal annealing. Mater Lett 151:126–129

[33] Li P, Sun H, Wang S, Hao X, Dong H (2020) Rotary friction welding of $AlCoCrFeNi_{2.1}$ eutectic high entropy alloy. J Alloys Compd 814:152322

[34] Kumar N, Komarasamy M, Nelaturu P, Tang Z, Liaw PK, Mishra RS (2015) Friction stir processing of a high entropy alloy $Al_{0.1}CoCrFeNi$. JOM 67(5):1007–1013

[35] Wei K, Lv M, Zeng X, Xiao Z, Huang G, Liu M, Deng J (2019) Effect of laser remelting on deposition quality, residual stress, microstructure, and mechanical property of selective laser melting processed Ti-5Al-2.5Sn alloy. Mater Charact 150:67–77

[36] Chen H, Gu D, Dai D, Xia M, Ma C (2018) A novel approach to direct preparation of complete lath martensite microstructure in tool steel by selective laser melting. Mater Lett 227:128–131

[37] Cao H, Dong X, Huang Q, Pan Z, Li J, Fan Z (2014) Effect of scanning speed during PTA remelting treatment on the microstructure and wear resistance of nodular cast iron. Int J Miner Metall Mater 21(4):363–370

[38] Yan M, Zhu WZ (1997a) Surface treatment of 45 steel by plasma-arc melting. Surf Coat Technol 91:183–191

[39] Wang M, Cui H, Wei N, Ding L, Zhang X, Zhao Y, Wang C, Song Q (2018) A new design of in situ Ti(C, N) reinforced composite coatings and their microstructures, interfaces, and wear resistances. ACS Appl Mater Interfaces 10:4250–4265

[40] Yan M, Zhu WZ (1997b) Surface remelting of Ni-Cr-B-Si cladding with a micro-beam plasma arc. Surf Coat Technol 92:157–163

[41] Zhang M, Li M, Chi J, Wang S, Ren L, Fang M (2019) Microstructure and tribology properties of in-situ MC(M:Ti, Nb) coatings prepared via PTA technology. Vacuum 160:264–271

[42] Li Y, Cui X, Jin G, Cai Z, Tan N, Lu B, Yang Y, Gao Z, Liu J (2017) Influence of magnetic field on microstructure and properties of TiC/cobalt-based composite plasma cladding coating. Surf Coat Technol 325:555–564

[43] Cheng JB, Xu BS, Liang XB, Wu YX (2008) Microstructure and mechanical characteristics of iron-based coating prepared by plasma transferred arc cladding process. Mater Sci Eng A 492:407–412

[44] Takeuchi A, Inoue A (2005) Classification of bulk metallic glasses by atomic size difference, heat of mixing and period of constituent elements and its application to characterization of the main alloying element. Mater Trans 46(12):2817–2829

[45] Gwalani B, Choudhuri D, Soni V, Ren Y, Styles M, Hwang JY, Nam SJ, Ryu H, Hong SH, Banerjee R (2017) Cu assisted stabilization and nucleation of $L1_2$ precipitates in $Al_{0.3}CuFeCrNi_2$ fcc-based high entropy alloy. Acta Mater 129:170–182

[46] Jones NG, Aveson JW, Bhowmik A, Conduit BD, Stone HJ (2014) On the entropic stabilisation of an $Al_{0.5}CrFeCoNiCu$ high entropy alloy. Intermetallics 54:148–153

[47] Jones NG, Christofidou KA, Stone HJ (2015) Rapid precipitation in an $Al_{0.5}CrFeCoNiCu$ high entropy alloy. Mater Sci Technol 31(10):1171–1177

[48] Jones NG, Frezza A, Stone HJ (2014) Phase equilibria of an $Al_{0.5}CrFeCoNiCu$ High Entropy Alloy. Mater Sci Eng A 615:214–221

[49] Pickering EJ, Stone HJ, Jones NG (2015) Fine-scale precipitation in the high-entropy alloy $Al_{0.5}CrFeCoNiCu$. Mater Sci Eng A 645:65–71

[50] Tsai MH, Yuan Y, Cheng G, Xu W, Tsai KY, Tsai CW, Jian WW, Juan CC, Shen WJ, Chuang MH, Yeh JW, Zhu YT (2013) Morphology, structure and composition of precipitates in $Al_{0.3}CoCrCu_{0.5}FeNi$ high-entropy alloy. Intermetallics 32:329–336

[51] Miao J, Pollock TM, Wayne Jones J (2009) Crystallographic fatigue crack initiation in nickel-based superalloy Rene 88DT at elevated temperature. Acta Mater 57:5964–5974

[52] Cui CY, Gu YF, Harada H, Ping DH, Sato A (2006) Microstructural evolution and mechanical properties of a Ni-based superalloy TMW-4. Metall Mater Trans A 37:3183–3190

[53] Jones NG, Izzo R, Mignanelli PM, Christofidou KA, Stone HJ (2016) Phase evolution in an $Al_{0.5}CrFeCoNiCu$ High Entropy Alloy. Intermetallics 71:43–50

[54] Li W, Liu P, Liaw PK (2018) Microstructures and properties of high-entropy alloy films and coatings: a review. Mater Res Lett 6(4):199–229

[55] An Z, Jia H, Wu Y, Rack PD, Patchen AD, Liu Y, Ren Y, Li N, Liaw PK (2015) Solid-solution CrCoCuFeNi high-entropy alloy thin films synthesized by sputter deposition. Mater Res Lett 3:203–209

[56] Katakam S, Joshi SS, Mridha S, Mukherjee S, Dahotre NB (2014) Laser assisted high entropy alloy coating on aluminum: microstructural evolution. J Appl Phys 116:104906

[57] He JY, Wang H, Huang HL, Xu XD, Chen MW, Wu Y, Liu XJ, Nieh TG, An K, Lu ZP (2016) A precipitation-hardened high-entropy alloy with outstanding tensile properties. Acta Mater 102:187–196

[58] Ganji RS, Sai Karthik P, Sankara Rao Bhanu K, Rajulapati KV (2017) Strengthening mechanisms in equiatomic ultra-fine grained AlCoCrCuFeNi high-entropy alloy studied by micro- and nanoindentation methods. Acta Mater 125:58–68

[59] Sriharitha R, Murty BS, Kottada RS (2014) Alloying, thermal stability and strengthening in spark plasma sintered AlxCoCrCuFeNi high entropy alloys. J Alloys Compd 583:419–426

[60] He JY, Liu WH, Wang H, Wu Y, Liu XJ, Nieh TG, Lu ZP (2014) Effects of Al addition on structural evolution and tensile properties of the FeCoNiCrMn high-entropy alloy system. Acta Mater 62:105–113

[61] Fu Z, Chen W, Wen H, Zhang D, Chen Z, Zheng B, Zhou Y, Lavernia EJ (2016) Microstructure and strengthening mechanisms in an FCC structured single-phase nanocrystalline $Co_{25}Ni_{25}Fe_{25}Al_{7.5}Cu_{17.5}$ high-entropy alloy. Acta Mater 107:59–71

[62] Liu WH, Wu Y, He JY, Nieh TG, Lu ZP (2013) Grain growth and the Hall-Petch relationship in a high-entropy FeCrNiCoMn alloy. Scr Mater 68:526–529

[63] Williamson GK, Hall WH (1953) X-ray line broadening from filed Al and W. Acta Metall 1:22–31

[64] Nie JF, Muddle BC (2008) Strengthening of an Al–Cu–Sn alloy by deformation-resistant precipitate plates. Acta Mater 56(14):3490–3501

[65] Wang ZG, Zhou W, Fu LM, Wang JF, Luo RC, Han XC, Chen B, Wang XD (2017) Effect of coherent $L1_2$ nanoprecipitates on the tensile behavior of a fcc-based high-entropy alloy. Mater Sci Eng A 696:503–510

[66] Booth-Morrison C, Dunand DC, Seidman DN (2011) Coarsening resistance at 400 °C of precipitation-strengthened Al–Zr–Sc–Er alloys. Acta Mater 59:7029–7042

[67] Wen H, Topping TD, Isheim D, Seidman DN, Lavernia EJ (2013) Strengthening mechanisms in a high-strength bulk nanostructured Cu–Zn–Al alloy processed via cryomilling and spark plasma sintering. Acta Mater 61(8):2769–2782

[68] Pollock TM, Argon AS (1992) Creep resistance of CMSX-3 nickel base superalloy single crystals. Acta Metall Mater 40(1):1–30